Chapter 1
Introduction and Literature survey

1.1 Introduction

A class of materials having general formula AB_2X_4 where A and B represent the divalent and trivalent cations, respectively, and X can be divalent anions (*e.g.* O, S, Se, Te, N) are defined as ***Spinels***. It can easily accommodate a large number of metals such as Ni, Zn, Mg, Al, Li, Mn, Co, Fe, Cr, Ti, Hg, Cd, Cu, *etc.*, which makes it chemically versatile along with flexibility in the crystal structure that gives rise to a variety of important chemical and physical characteristics [1–3]. Besides the synthetic spinels, spinels also exist in the mantle and crystal rock of the earth as a natural mineral[4,5]. In fact, the name "spinel" was adopted from the Latin word ‘spinella’ after the natural mineral spinel, $MgAl_2O_4$ because of the resemblance of their crystal structure.

1.2 Structure of spinel oxide

Bragg and Nishikawa determined the structure of spinel oxide in 1915, using the X-ray diffraction technique [6,7]. The majority of spinel oxides consist of cubic phase with the space group $Fd\bar{3}m$ (space group number: 227). A cubic unit cell of spinel oxide primarily comprises 4 primitive tetrahedral unit cells (**Figure 1.1)** [8]. Each tetrahedral unit cell contains 2 formula units (Z) or the molecular unit (AB_2O_4). Hence, there are 4×2 = 8 formula units present in a cubic unit cell. The oxygen anions are packed in a cubic closed packed (*ccp*) arrangement which results in a face-centered cubic (*fcc*) Bravais lattice of the conventional cubic unit cell [9,10]. **Figure 1.2** depicts the voids, cations, and anions in a unit cell of spinel.

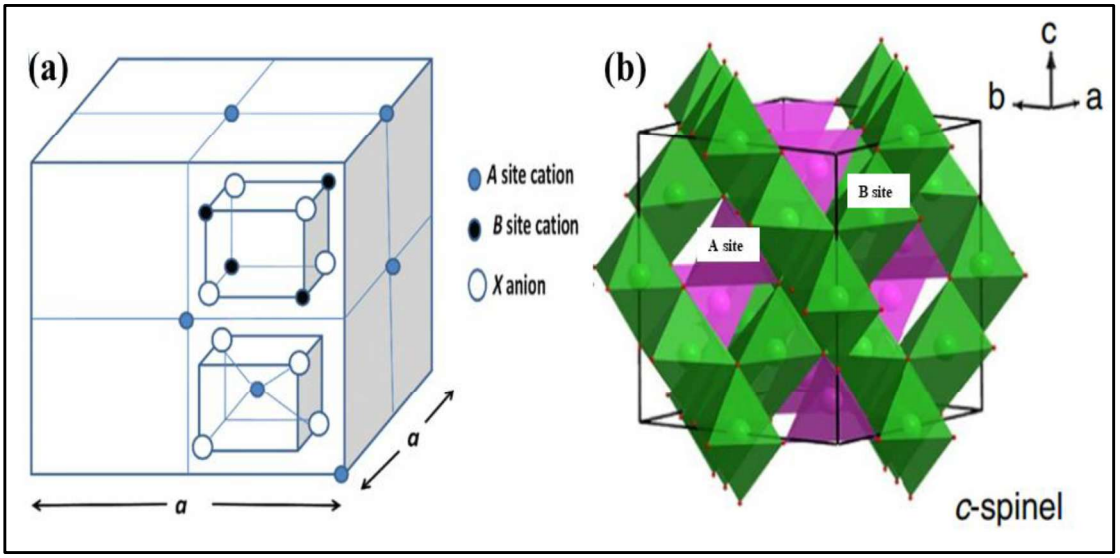

Figure 1.1: (a) Cubic unit cell of spinel oxide comprising four primitive tetrahedral unit cell. (b) A depiction of tetrahedral (A) and octahedral (B) sites formed by oxygen anions (small red spheres).

Cations can occupy 1/8th of 64 *A* sites and 1/2 of 32 *B* sites, resulting in a total of 72 vacant *A* and *B* sites. The *A* and *B* sites vacancies are denoted as Δ and $\square$, respectively. The positive charge of *A* and *B* site cations is balanced by 32 oxygen anions in a unit cell. The *A* site tetrahedron and *B* site octahedron shares oxygen anion corners with each other, and individual *A* site tetrahedron do not share any corner or O-O edge with the other *A* site tetrahedron. The six out of twelve O-O edges of *B* site octahedron are shared with the neighboring *B* sites. The choice of origin in a unit cell could be at vacant *A* and *B* sites or cations occupied or at the position of oxygen anion.

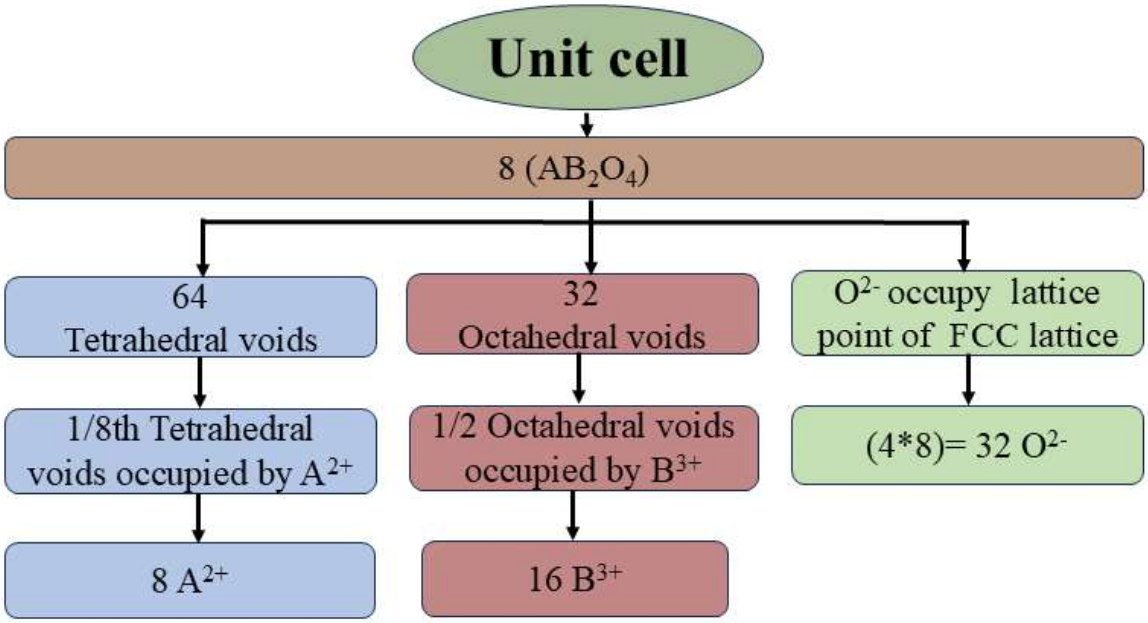

Figure 1.2: Number of voids, and distribution of cations and anions in unit cell of spinel.

1.2.1 Classification of spinel oxides

While several factors affect the physical properties of spinel oxides, the chemical identity of cations and their distribution in *B* and *A* sites are key factors among them. The distribution of cations can be determined using various techniques such as X-ray absorption fine-structure (XAFS) and X-ray diffraction, *etc*. The cation distribution in spinel oxides can be stated as:

$$(A_{1-i}^{2+}\ B_i^{3+})\ [(A_i^{2+}B_{2-i}^{3+}]O_4 \qquad (1.1)$$

where the parentheses signify the *A* site, square brackets signify the *B* site, and *i* is the inversion parameter. Based on the value of inversion parameter *i*, spinels can be classified into three groups: Normal ($i = 0$), Inverse ($i = 1$) and Mixed spinel ($0 < i < 1$). In normal spinel where *i* value is 0, all divalent cations reside in the *A* site and all trivalent cations reside in the *B* site [11–13]. In inverse spinel where *i* value is 1, all the divalent cations occupy the *B* site and the trivalent cations are equally distributed between the *A* and *B* sites [14,15].

In mixed spinel oxides where *i* value varies between 0 and 1, cations do not show any preference for the particular site and their distributions are random[8,16]. **Table 1.1** gives some examples of normal, inverse, and mixed spinels structure [16]. The cation distribution in spinel oxides can be governed by several factors such as temperature, cationic radii, electrostatic energy of lattice, crystal field stabilization energy, *etc* [9]. The cation distribution estimation based on the crystal field stabilization energy (CFSC) has shown a notable similarity with the experimental observation, which makes it a prominent factor in determining the cation distribution.

Table 1.1: Examples of spinel oxides with normal, inverse, and mixed cation distribution.

Spinel	**Type**	**Distribution**
$CoCr_2O_4$	Normal	$(Co_1^{2+})\ [Cr_2^{3+}]$
$NiCr_2O_4$		$(Ni_1^{2+})\ [Cr_2^{3+}]$
$MnCr_2O_4$		$(Mn_1^{2+})\ [Cr_2^{3+}]$
$CoMn_2O_4$		$(Co_1^{2+})\ [Mn_2^{3+}]$
$CoFe_2O_4$	Inverse	$(Fe_1^{3+})\ [Co_1^{2+}Fe_1^{3+}]$
$CuFe_2O_4$		$(Fe_1^{3+})\ [Cu_1^{2+}Fe_1^{3+}]$
$Li_{0.5}Fe_{2.5}O_4$		$(Fe_1^{3+})\ [Li_{0.5}^{1+}Fe_{1.5}^{3+}]$
$MgFe_2O_4$	Mixed	$(Mg_{0.1}^{2+}Fe_{0.1}^{3+})\ [Mg_{0.1}^{2+}Fe_{1.9}^{3+}]$
$MnFe_2O_4$		$(Mn_{0.15}^{2+}\ Fe_{0.85}^{3+})\ [Mn_{0.85}^{2+}\ Fe_{1.15}^{3+}]$

1.2.2 Crystal field theory

All *d* orbitals (d_{xy}, d_{xz}, d_{yz}, $d_{x^2-y^2}$, and d_{z^2}) are degenerate in the absence of any external interaction. However, when degenerate *d* orbitals are positioned in a crystal lattice of ions, they no longer remain degenerate and split depending upon the symmetry of the electric field due to the surrounding ions[17]. In the crystal field theory, the average of such electric field is called the crystal field and the interaction between the *d* orbitals and the orbitals of the surrounding ions is basically of an electrostatic repulsion nature.

For example, in a tetrahedral environment in spinel oxides, d_{xy}, d_{yz} and d_{zx} orbitals of a central atom are in close proximity to the 2*p* ($2p_x$, $2p_y$, and $2p_z$) orbitals of tetrahedral oxygen anions, therefore, they become destabilized [17,18]. On the other side, $d_{x^2-y^2}$ and d_{z^2} orbitals do not effectively interact with these 2*p* orbitals and become stabilized. As a result, *d* orbitals in a tetrahedral environment is split into two groups: doubly degenerate *e* ($d_{x^2-y^2}$, d_{z^2}) orbitals at lower energy and the triply degenerate t_2 (d_{xy}, d_{yz}, d_{zx}) orbitals at higher energy. For the octahedral environment of surrounding oxygen anions, the $d_{x^2-y^2}$ (along *x* and *y* axes) and d_{z^2} (along *z* axis) orbitals predominantly overlap with the $2p_x$, $2p_y$, and $2p_z$ orbitals of oxygen anions, hence become destabilized. The d_{xy}, d_{yz}, and d_{zx} orbitals which are in between the *x*, *y,* and *z* axes, do not directly overlap with the 2*p* orbitals of oxygen anions, hence become stabilized [18,19]. Consequently, in an octahedral environment, *d* orbitals are split into two groups: the triply degenerate t_{2g} (d_{xy}, d_{yz}, d_{zx}) orbitals at lower energy and the doubly degenerate e_g (d_{x2-y2}, d_{z2}) orbitals at higher energy. **Figure 1.3** shows the splitting of degenerate 3*d* orbitals into different groups based on the tetrahedral and octahedral environment of surroundings anions. The CFSE, Δ (or 10 Dq) is calculated as the energy difference between the doubly and triply degenerate orbitals. For the same *d* configuration, Δ in the *A* site is 4/9 fraction of that in the *B* site. **Table 1.2** provides the Δ values for some transition metal cations occupying the *A* and *B* sites [16]. The difference in Δ of *A* and *B* sites is known as octahedral site preference energy (OSPE), and it is more suitable to use OSPE for determining the occupancy of transition metal cations in a binary spinel oxide. Generally, transition metal cations having the highest OSPE tend to favor occupying the *B* site.

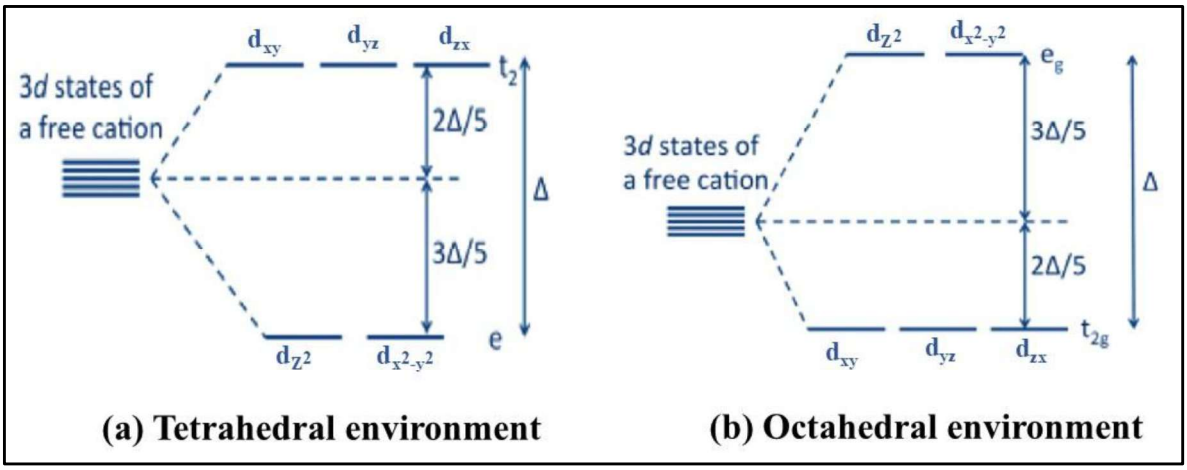

Figure 1.3: Energy level diagram for the tetrahedral (A) and octahedral (B) environment of oxygen anion of spinel oxides.

Table 1.2: Transition metal cations with crystal field stabilization energy (CFSE) in A and B sites.

Cations	**No. of 3d electrons**	**Theoretical CFSE in terms of Dq**		**Experimental OSPE in eV**
		***B* site**	***A* site**	
Ti^{3+}	1	4	6	0.33
V^{2+}	2	8	12	0.53
Cr^{3+}	3	12	8	2.02
Mn^{3+}	4	6	4	1.10
Fe^{3+} Mn^{2+}	5	0	0	0 0
Fe^{2+}	6	4	6	0.17
Co^{2+}	7	8	12	0.09
Ni^{2+}	8	12	8	0.99
Cu^{2+}	9	6	6	0.68
Zn^{2+}	10	0	0	0

1.2.3 Jahn-Teller distortion

According to the electronic configuration of 3*d* orbitals, t_{2g} / e_g and e / t_2 orbitals could be degenerate which may cause the lattice destabilization. To stabilize the lattice, the electronic degeneracy can further be removed by a geometrical distortion known as Jahn-Teller (*J-T*) distortion [20,21]. For example, in the case of $3d^4$ configuration in the high spin state in an octahedral environment, three electrons occupy the lower energy t_{2g} orbitals with no orbital degeneracy, whereas the fourth electron occupying one of two available e_g ($3d_{x^2-z^2}$ and $3d_{z^2}$) orbitals show the doubly degenerate state. To lift the orbital degeneracy in e_g orbitals, the *J-T* distortion stretches the octahedron along the positive z-axis and this process results in the lower energy of $3d_{z^2}$ orbital due to smaller overlapping with the orbitals of surrounding anions. So, the fourth electron occupies the $3d_{z^2}$ orbital and reduces the overall energy of the system [20]. This process of octahedron stretching due to distortion is shown in **Figure 1.4**. On the other hand, in some cases, the lifting of orbital degeneracy is attained by compression of the octahedron along the *z*-axis, where the $3d_{x^2-z^2}$ orbital with lower energy is occupied by the fourth electron instead of the $3d_{z^2}$ orbital with higher energy (**Figure 1.4**).

Only certain electronic configurations of 3*d* orbitals are compatible to the *J-T* distortion, while others are not affected by it. Moreover, the degree of *J-T* distortion depends on the presence of electronic degeneracy in non-bonding and antibonding orbitals. In the octahedral environment, electronic configurations $3d^4$ (t_{2g}^3, e_g^1) and $3d^9$ (t_{2g}^6, e_g^3) are expected to show large *J-T* distortion because of the presence of degeneracy in their antibonding e_g orbitals [20,21]. Other configurations such as $3d^1$ ($t_{2g}^1 e_g^0$), $3d^2$ (t_{2g}^2 e_g^0), $3d^6$ (t_{2g}^4 e_g^2) and $3d^7$ (t_{2g}^5 e_g^2) show small *J-T* distortion because of the presence of degeneracy in their non-bonding t_{2g} orbitals [20] . In the tetrahedral environment, t_2 orbitals are antibonding whereas *e* orbitals are non-bonding. Here the degeneracy in antibonding t_2

orbitals is expected to show large *J-T* distortion. The spinel oxides with electronically degenerate orbitals manifest the *J-T* distortion as a structural phase transition, typically from higher symmetry cubic phase to lower symmetry tetragonal phase. In normal spinel Mn_3O_4 which can also be denoted as $(Mn^{2+})[Mn^{3+}]_2O_4$, the *B* site Mn^{3+} cation is *J-T* active (electronically degenerate e_g^1 orbital) [22,23]. It is also reported that all the Mn rich

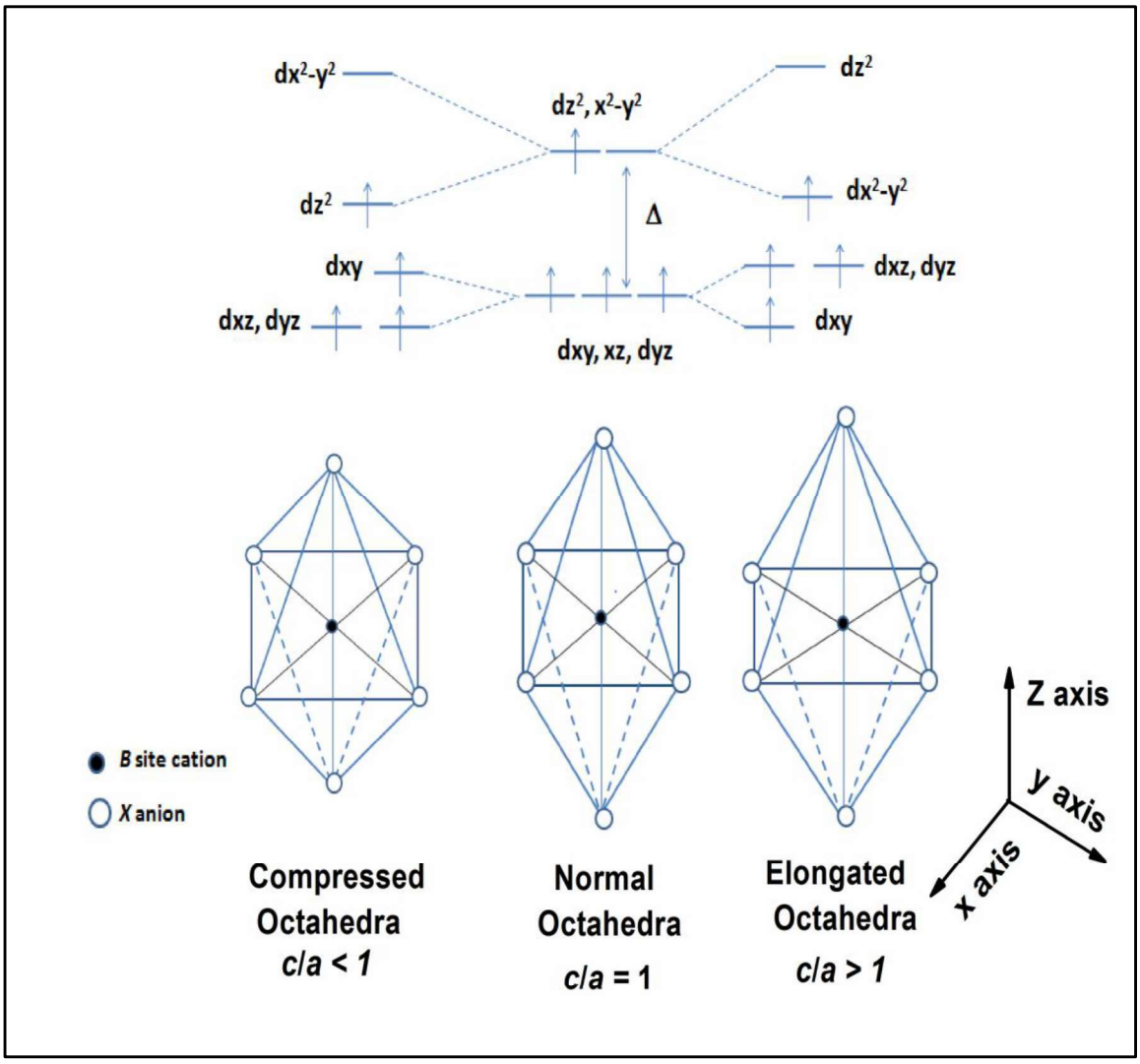

Figure 1.4: The splitting of t_{2g} and e_g orbitals of d^4 configuration due to the *J-T* distortion.

compound like $ZnMn_2O_4$, $MgMn_2O_4$, $FeMn_2O_4$, $NiMn_2O_4$ and $CoMn_2O_4$, where Mn^{3+} occupied more than 60-65% of the octahedral site, shows the octahedral distortion due to the Jahn-Teller effect[24–26].

1.3 Magnetism in spinel oxides

Magnetite (Fe_3O_4) was the first known magnetic material, used for navigation since 600 B.C. In the 20th century, potential of spinel oxides revolutionized technologies like data storage, medical imaging, and drug delivery [27,28]. The magnetic behavior of spinel oxides depends on the cationic arrangement in A and B sites, making their study vital for advanced applications.

1.3.1 Magnetic exchange interactions

The exchange interaction among the magnetic cations is responsible for the emergence of the phenomenon of long-range magnetic ordering below a critical temperature in a magnetic system. This interaction is a quantum mechanical effect, stemming from a combination of the Pauli exclusion principle and Coulomb's law. Heisenberg exchange Hamiltonian proposed in 1928 [29], stated the exchange interaction energy, E_{ex} between the atoms *i* and *j* by the following equation.

$$E_{ex} = -2j \sum_{i \neq j} S_i . S_j \qquad (1.2)$$

where *J* presents the exchange integral between the spins S_i and S_j of i^{th} and j^{th} atoms, respectively. In a real-world problem, the calculation of *J* could be challenging, though some conclusions could easily be drawn from its sign. In ferromagnets (FM) where $J > 0$, the exchange interaction between the magnetic ions couple their spins in a parallel arrangement with each other as it leads to a minimum in E_{ex}. In ferrimagnets (FIM) and antiferromagnets (AFM) where $J < 0$, the antiparallel arrangement of neighboring spins is energetically more favorable and stable [29]. The exchange interaction at the microscopic level is divided into different classes based on the possibility of direct or indirect overlap of electron wave functions of interacting magnetic ions. Here, some important types of exchange interactions are discussed briefly.

1.3.1.1 Direct exchange interaction

When the magnetic ions at two different sites interact through the overlapping of their electron wave functions, is known as a direct exchange interaction. For the direct exchange interaction to occur, the interacting magnetic ions must be close to each other. Pauli's exclusion principle describes that the electrons having parallel spins stay away from each other to minimize the Columbic energy. Hence, the direct exchange interaction is only found in the antiparallel arrangement of spins of neighboring magnetic ions. However, this interaction is very rarely brought into the picture while determining the magnetic properties, due to the lack of sufficient overlapping of electron wave functions in them [18,19]. For instance, in rare earth and transition metals, the wave function of 3*d* or 4*f* electrons decreases exponentially with the increase in distance from the nucleus and results in a very small exchange constant *J* which is insufficient to provide the necessary exchange coupling [19]. Thus, it is important to consider the indirect type of exchange interaction in magnetic materials.

1.3.1.2 Superexchange interaction in spinel oxides

In superexchange interaction, two next to nearest neighbor magnetic cations interact by a non-magnetic anion such as oxygen in the case of oxides. This interaction is a dominant type of exchange interaction in insulators and semiconductors where the orbitals of magnetic cations are highly localized and overlap with the orbitals of the intermediary non-magnetic anion. Unlike weak direct exchange interaction which is a short-range interaction, this interaction is a strong and long-range interaction. In 1934, Kramers first proposed the concept of superexchange interaction while investigating the magnetic properties of MnO system [30]. He noticed that Mn ions in MnO were interacting with each other even though they were separated by an intermediary non-magnetic O^{2-} ion. Later on, a set of semi-empirical rules are developed over a period of time by

Goodenough and Kanamori [22,31–33] . These semi-empirical rules are now referred to as the famous Goodenough-Kanamori rules which have successfully justified the magnetic properties of several magnetic materials. The main feature of these rules is that they take into account the occupancy of *d*-shells of magnetic cations along with the magnetic cation-ligand-magnetic cation bond angle. According to these rules, if the bond angle (magnetic cation-ligand-magnetic cation) is 180^0 and the *d*-shells of magnetic cations are partially filled, then the superexchange interaction is strongly antiferromagnetic. However, this interaction is much weaker and ferromagnetic in the case of 90^0 bond angle with partially filled *d*-shells.

For the spinel oxides, where magnetic cations among *A* and *B* sites interact with each other via. O^{2-} anions [22], superexchange interaction of *A-O-B* network dominates over the other possible superexchange interactions such as *A-O-A* and *B-O-B*. The *A-O-B* bond angle is generally found to be around 125^0 and results in an AFM superexchange interaction between the *A* and *B* sites magnetic cations [33]. For *B-O-B* network, the bond angle is about $90^{0,}$ and consequences in an FM superexchange interaction.

1.3.2 Ferrimagnetism

Ferrimagnetism is a permanent type of magnetism where the magnetic moments having different magnitudes align antiparallel and give a net magnetization. Ferrimagnetic (FIM) materials show spontaneous magnetization below a critical temperature known as the FIM curie temperature, T_C [29]. Above T_C, the FIM materials exhibit the paramagnetic behavior as shown in **Figure 1.5**. Cubic ferrites were the first spinel oxides to be identified with this type of magnetism. In a typical FIM material, different sublattices of magnetic cations are crystallographically different which causes the different molecular fields to act on different sublattices [34]. Thus, individual sublattice magnetization and its

temperature dependence also differ. For example, in AB_2O_4 spinel oxide with two different sublattices, the local molecular field acting on *A* sublattice would differ from the local molecular field acting on *B* sublattice even though both sublattices have identical magnetic cations [29]. In this context, a molecular field theory proposed by Néel could be useful to understand the different molecular fields and their role in determining the temperature dependence of sublattice magnetization. As per Néel's theory, local molecular fields, H_A and H_B acting on the *A* and *B* sublattices, respectively, are given by

$$H_A = \gamma(\alpha M_A - M_B) \tag{1.3}$$

$$H_B = -\gamma(M_A - \beta M_B) \tag{1.4}$$

Where, M_A and M_B are the magnetizations of *A* and *B* sublattices, respectively. While α is a molecular field coefficient for *A*-*A* intra-sublattice interaction, β is a molecular field coefficient for *B*-*B* intra-sublattice interaction. Both α and β are normalized by the molecular field coefficient, γ for the *A*-*B* exchange interaction. Both magnetic field and temperature dependent magnetizations of *A* and *B* sublattices depend on the Brillouin function $B_S(x)$ and are given as:

$$M_A = \lambda N g \mu_B S_A B_{S_A}\left(\frac{g\mu_B S_A (H_A + H)}{\kappa_B T}\right) \tag{1.5}$$

$$M_B = \delta N g \mu_B S_B B_{S_B}\left(\frac{g\mu_B S_B (H_B + H)}{\kappa_B T}\right) \tag{1.6}$$

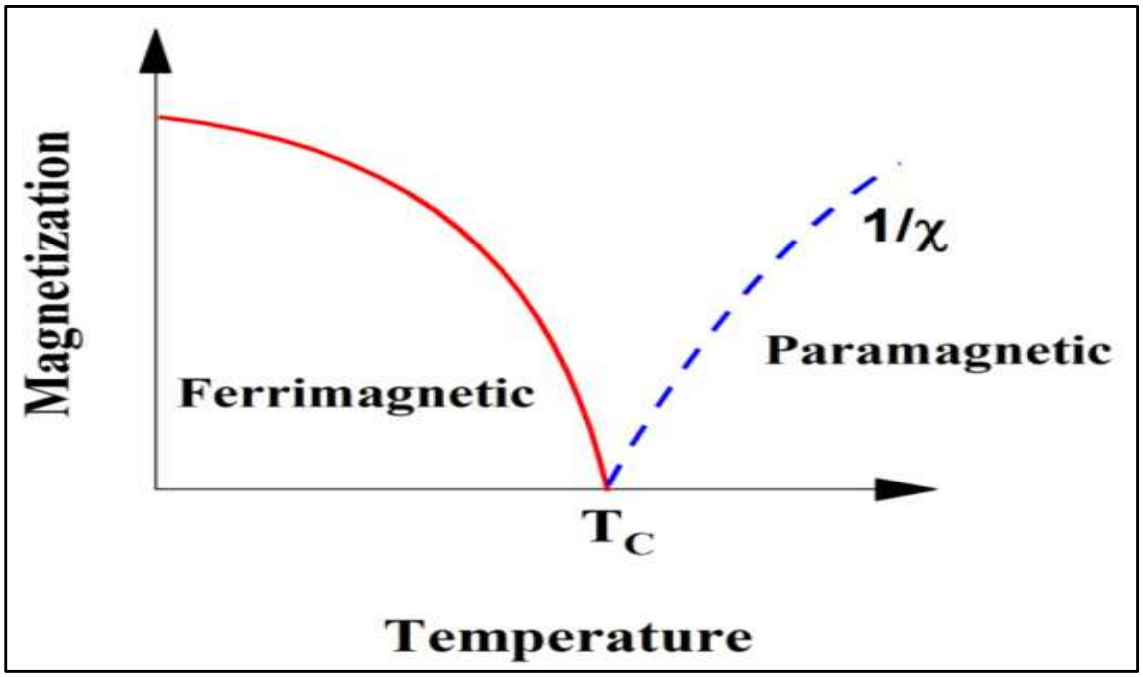

Figure 1.5: Magnetization and susceptibility depending on temperature in a typical ferrimagnetic material.

Where N represents the number of magnetic cations per unit volume. The spin angular momentum corresponding to the A and B sites are given by S_A and S_B, respectively. The fractional molar concentrations at A and B sites are denoted by λ and δ, respectively, with $\lambda + \delta = 1$. The sublattice magnetization is given by equation (1.5) and equation (1.6) depending on the parameters α, β, γ, S_A, S_B, λ and δ. The curve shape for A sublattice will differ from the curve shape for the B sublattice. Subsequently, the resultant magnetization curve is the difference between these two. Consequently, a small change in the curve shapes of the sublattice can introduce an unusual resultant magnetization curve. Thus, the FIM materials are very fascinating magnetic materials where often the net magnetization dies out below the transition temperature and subsequently becomes negative [35]. The temperature at which resultant magnetization dies out is known as the compensation temperature (T_{comp}), at this point opposing sublattice magnetizations are

exactly balanced **(Figure 1.6)**. Above and below the compensation temperature, one sublattice magnetization dominates over the other. All the chromium based spinel, fall into this category.

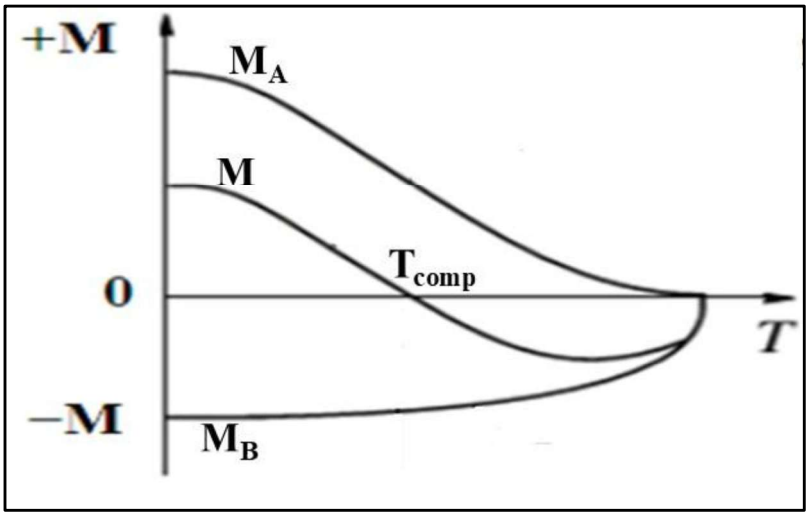

Figure 1.6: A and B sublattice magnetizations showing the spontaneous magnetization. The resultant magnetization curve (M) exhibiting the compensation temperature.

1.3.3 Geometrical magnetic frustration and Y-K spin

If the interactions between the magnetic cations are incompatible with the lattice symmetry, then it results in geometrical magnetic frustration (GMF). The simplest example of GMF is a triangular lattice with three spins as shown in **Figure 1.7**. If two of the spins are aligned antiparallel to each other on the two vertices to form an AFM arrangement, then it would be impossible for the third spin to align antiparallel simultaneously to the other two spins. Thus, the energy of all interactions cannot be minimized simultaneously which simply means that the AFM ordering is energetically not compatible with the triangular lattice. Other than triangular lattice, GMF is also being studied on the network of vertex sharing triangles known as kagome lattice, and the network of corner-sharing tetrahedrons forming the pyrochlore lattice [36].

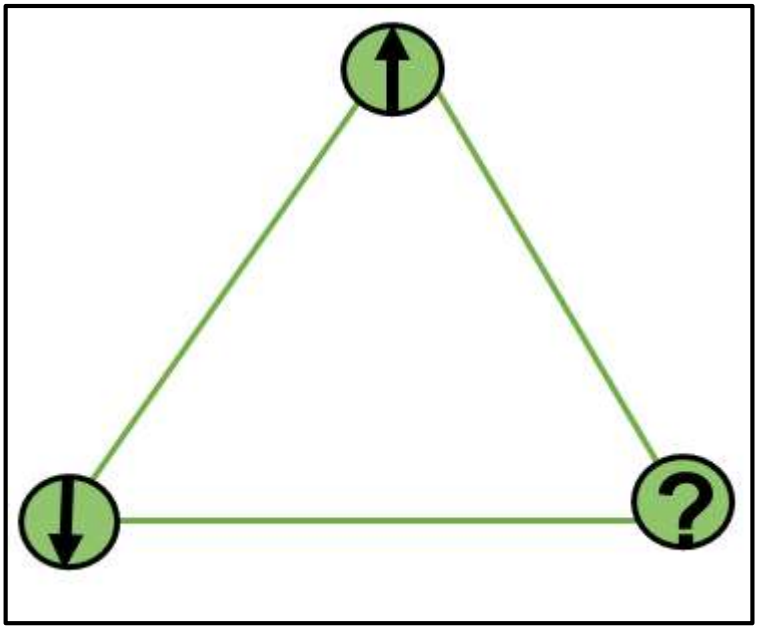

Figure 1.7: Magnetic frustration on a triangular lattice. Three neighbouring spin cannot form pairwise antiferromagnetic order, causing magnetic frustration.

Yafet and Kittel proposed a new model based on triangular spin arrangement when Neel's theory fails to explain the change in magnetization with the help of antiparallel spin arrangement in some spinels. They postulated that when a strong negative interaction exists within the B sublattice the two equivalent B_1 and B_2 get spontaneously magnetized. The magnetizations are not exactly antiparallel, but are aligned at an angle. This triangular arrangement within the lattice results in values of change in magnetization of same order and magnitude as those stated by Neel's model. Such Type of non-collinear arrangement of spins are known as Yafet – Kittel spin structure[37].

1.3.4 Exchange bias

In the exchange bias phenomenon, unidirectional exchange anisotropy is developed at the boundary of the reversible and irreversible magnetic phases, resulting in a shifting of the hysteresis (M-H) loop along the magnetic field axis. Meiklejohn and Bean discovered this phenomenon in 1956 while investigating the magnetic hysteresis behavior of a

bilayer system composed of ferromagnetic (FM) core of Co particles coated with the partially oxidized AFM layer of CoO particles[38]. It was observed that the center of the hysteresis loop shifted toward the negative field direction when the field cooled below the Néel temperature, T_N of CoO layer (AFM). Since their discovery, a multitude of magnetic systems such as FIM/AFM, FIM/FIM, FIM/FM, spin-glass/FM, *etc.*, have shown the exchange bias effect [39–42]. In a recent development, exchange bias has been classified into two broad categories, conventional and spontaneous. The shift in hysteresis loop under field cooled condition is considered as conventional exchange bias (CEB), whereas under the zero-field cooled condition it is considered as the spontaneous exchange bias (SEB)[43–48]. The shift in M-H loop also known as exchange bias field (H_{EB}) can be calculated as $H_{EB} = (H_{C1} + H_{C2})/2$, where H_{C1} and H_{C2} are the coercive fields associated with the descending and ascending branches of the hysteresis loop, respectively [49]. The sign of H_{EB} could be either positive or negative depending upon the direction of shift along the field axis. In this context, based on a theoretical approach, Nogues has suggested that the ferromagnetic coupling at the FM/AFM interface is responsible for the negative H_{EB}, whereas the antiferromagnetic coupling for the positive H_{EB} [50].

Although the mechanism behind the exchange bias phenomenon varies from one system to another, a typical example of AFM/FM bilayer system under field cooled condition could be very useful for describing it [39]. **Figure 1.8** shows the schematic diagram of field cooled (FM) hysteresis loop of AFM/FM bilayer system and the associated spin configurations at the different stages in both FM and the AFM layers [39]. During the field cooling in the temperature range of $T_N < T < T_C$, while FM spins align along the field direction, the AFM spins remain random due to their PM state (**Figure 1.8(a)**). When the AFM/FM bilayer is field cooled through the T_N, the spins of AFM and FM interact with

each other at the interface in such a way that the first layer of AFM spins aligns parallel to the FM spins (**Figure 1.8(b)**). So, there is an FM interaction at the FM/AFM interface, however, spins deep inside the AFM layer simply follow the AFM ordering. During the magnetic field reversal stage shown in **Figure 1.8(c)**, while the FM spins try to align along the reversed field direction, AFM spins due to large magnetic anisotropy remain in the original direction. Thus, the microscopic interaction at FM/AFM interface resists the FM spins from rotating along the field direction. In other words, interfacial AFM spins with strong anisotropy provide a microscopic torque on reversible FM spins to conserve their original direction. Thus, a unidirectional anisotropy develops at the FM/AFM interface and a large negative field is required to align FM spins in FM/AFM bilayer system compared to the case of isolated FM substance and to attain the stage shown in **Figure 1.8(d)**. As a result, the coercive field associated with the descending branch increases. On the other hand, while changing the magnetic field in the positive direction, FM spins easily align along the field direction. The unidirectional anisotropy at the interface now exerts a microscopic torque in the applied field direction (**Figure 1.8(e)**) and results in a reduced coercive field associated with the ascending branch. The net effect is the shifting of hysteresis loop along the negative field direction. In the above process, we have considered the FM coupling at the interface that gives rise to the shifting of the hysteresis loop along the negative field axis. If the coupling at the interface is AFM, one would expect the shifting of the loop along the positive field axis.

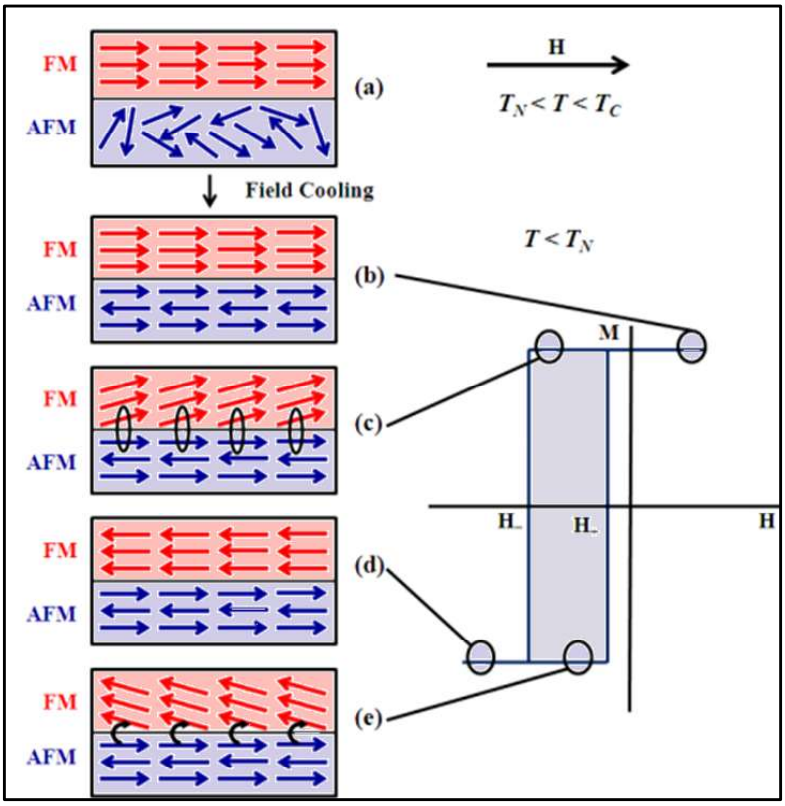

Figure 1.8: Illustration for the exchange bias mechanism. The spin arrangement near the FM-AFM interface coupling is illustrated at various stages of the hysteresis loop shift.

Apart from the shifting along the loop axis, shifting along the negative field axis is also reported for few systems. Thus, in such system vertical magnetization shift (VMS) is observed along with exchange bias (H_{SEB} and H_{CEB}). Exchange bias can be observed for many materials [51,52] , while vertical magnetization shift (VMS) is rarely observed [53–58]. VMS is defined as the complete loop shifting on the magnetization axis and has the potential to revolutionize the future of ultrahigh-density magnetic recording technology [59]. It is crucial to discuss the relationship between VMS and pinning strength. Mumtaz et al. discussed VMS in $CoFe_2O_4$ nanoparticles and further observed a different behavior of conventional exchange bias H_{CEB} and VMS with particle size and cooling field which suggest the variation in pinning strength. H_{CEB} and VMS are related to weakly and strongly pinned uncompensated spins respectively[60]. Tian et al. reported a vertical shift

(M_E) of 0.15 emu/g in $NiFe_2O_4$ nanoparticles and suggested that the vertical shift is due to the exchange coupling between the spin glass-like phase and the ferrimagnetic phase[61].

1.4 Literature review on Co-Mn based spinel

Transition metal-based spinels, particularly cobalt manganese oxides ($Co_xMn_{3-x}O_4$) are of great interest because of their remarkable structural and physical properties along with potential applications in magnetic recording, energy storage, batteries, supercapacitors, and catalysis etc. [62–70]. Here, a concise overview of the literature reported on the synthesis, structure, local structure and microstructure transitions along with properties of Co-Mn based spinel is presented. The emphasis has been given to the structural and magnetic properties of $Co_xMn_{3-x}O_4$ and doped $CoMn_2O_4$.

1.4.1 Synthesis of the Co-Mn based spinel

Spinels can be synthesized through a variety of techniques with controllable morphologies such as size, shape, and growth of the particles by adjusting the synthesis parameters. Generally, a simple thermal decomposition, combustion, co-precipitation, microwave, and sol-gel synthesis techniques are employed to prepare the spinel.

Thermal decomposition is mostly used where nitrate decomposition and nitrate combustion occur [71–74]. By varying the precursor (metal nitrates), different spinels such as $CoCr_{2-x}V_xO_4$, $Mn_xCo_{3-x}O_4$, and $Cu_xMn_{3-x}O_4$, can be synthesized[75–77]. Rios et al., have prepared $Mn_xCo_{3-x}O_4$ (x = 0, 0.25, 0.5, 0.75, 1) by thermal decomposition using $Mn(NO_3)_2{,}4H_2O$, $Co(NO_3)_2{,}6H_2O$ and HNO_3 [75]. The thermal decomposition of cobalt and manganese acetylacetonate, as well as the thermal decomposition of oxalate-based network, are also used for the preparation of Co-Mn based spinel particles [78,79] Using acetylacetonate precursor, particles of 6.7 to 12 nm have been obtained while 8 to 40 nm particles are obtained using oxalate-based network[79,80].

Another chemical route for the synthesis of spinels is the combustion technique, a quick synthesis method that uses exothermic reactions to speed up the reaction rates. It is also known as self-propagating high temperature synthesis and introduced by Merzhanov et al. in 1960s [81,82]. Kutty et al. have utilized this technique to synthesize Co-Mn based spinel where $Co(NO_3)_2 \cdot 6H_2O$, $MnCl_2 \cdot 4H_2O$ and $C_2H_5NO_2$ are chosen as the precursors. The pH of final solution is found to be 7 heated to 80 °C followed by firing at > 100 °C and calcination at 700 °C for 10 h. The obtained spinel particles have average diameter of 150 nm[83].

Sol−gel is another commonly used technique for the synthesis of spinel nanoparticles [84–86]. In this method, metal salts are typically used as precursors. Citric acid [87,88], ethylenediamine tetraacetic acid[89,90], propionic acid[91,92], ethylene glycol[93,94], glycine[95], glacial acetic acid[96,97], P123[96,97], or resorcinol/ formaldehyde[98] are generally used as chelating agents. Joelle C.W. Mah et al., have used nitrate precursor with $C_6H_8O_7 \cdot H_2O$ and $C_2H_6O_2$ to prepare the Co-Mn based spinel. On calcination at 600 °C, 700 °C, and 800 °C, the particle of average crystallite size of 25, 23, and 21 nm, respectively have been obtained [99].

Coprecipitation, has also been used to synthesize the spinels. It has several advantages over other techniques such as cheapness, control over the particle size and surfactant-free synthesis. Coprecipitation synthesized $CoMn_2O_4$ and $MnCo_2O_4$ where $MnCl_2 \cdot 4H_2O$ and $Co(NO_3)_2 \cdot 6H_2O$ used as precursors and ammonium carbonate $(NH_4)_2CO_3$ as precipitating agent, shows the pure tetragonal (100-200 nm particle size) and cubic phase (40- 70 nm particle size), respectively [3]. Hosseini et al. have prepared $CoMn_2O_4$ using nitrate salts of Mn and Co with NH_4OH as a precipitating agent at pH 8.3 and the sample has been found to coexist in normal (tetragonal phase) and inverse spinel (Cubic phase)[26]. Apart from pH and calcination temperature, Li et al. have obtained

$CoMn_2O_4$, $Mn_{1.50}Co_{1.50}O_4$, and $MnCo_2O_4$ in both pure cubic and tetragonal phases just by changing the precursor mixing sequence where nitrate precursors and NH_4OH as precipitating agent are used [2]. Thus, by changing the synthesis technique and parameters, one can obtain different structures and morphologies of Co-Mn based spinels, which influence the physical properties.

1.4.2 Structural phase transitions in Co-Mn based spinel

Co-Mn based spinels have invoked a broad research interest, as both Co and Mn can have multiple valences. Both cations can occupy octahedral and tetrahedral site, having a cooperative Jahn-Teller (*J-T*) distortion induced structural phase transformations. The structural phase transitions have been observed in $Co_xMn_{3-x}O_4$ just by changing the preparation method and varying the x from 0.00 to 2.00. The crystal structure of the haussmanite $x = 0$ (Mn_3O_4) exibits a tetragonal distortion of the spinel structure ($I41/amd$ space group), which arises from the presence of Mn^{3+} in the B site. This distortion is driven by the Jahn-teller effect associated with the Mn^{3+} in B site (d^4 configuration of high spin state) [100]. The minimum required concentration of Mn^{3+} in the B site is about 55% for J-T distortion. [101]-[102]. Structural transformation has been reported when non-magnetic cations like Mg/Zn, and magnetic cations like Ni, Fe, and Co are doped in Mn_3O_4 [24,103–107]. Mehdaoui et al. have reported the structural transformation for $Mg_xMn_{3-x}O_4$ where x varies from $x = 0.00$ to 2.00. For $0 \leq x \leq 0.9$, pure tetragonal phase (space group $I41/amd$) is observed with decrease in c/a ratio on increasing x. For $1.5 \leq x \leq 2$, the compounds form in the cubic structure (space group $Fd\bar{3}m$), where the lattice parameter decreases with an increase in x. The structural ionic formula is then $(Mg^{2+})_A[Mg^{2+}_{x-1}Mn^{3+}_{2(2-x)})Mn^{4+}_{x-1}]_BO_4$ for pure cubic compositions. Although intermediate compositions ($1 \leq x \leq 1.4$) have coexistence of both the cubic and tetragonal phases. For these compositions, the tetragonal symmetry changes continuously towards

cubic symmetry when x increases [106]. For $Zn_xMn_{3-x}O_4$ having the cationic distribution $(Zn^{2+})_A[Zn^{2+}\ Mn^{3+}Mn^{4+}]_BO_4$, there is no structural change when x is varying from 0.00 to 1.29, however, the reduction in tetragonality (c/a) from 1.64 to 1.55 is observed for x = 0.30 to1.29 [107]. Furthermore, the doping of Fe in Mn_3O_4 induces the substitution of Mn^{3+} at octahedral sites by Fe^{3+} resulting in small but measurable changes in the unit cell parameters, demonstrating a decrease of J-T distortion with increasing Fe^{3+} concentrations up to $(Mn^{2+}_{0.943}\ Fe^{2+}_{0.057})_A[Mn^{3+}_{0.880}\ Fe^{3+}_{0.120}\ ]_BO_4$. Finally, $MnFe_2O_4$ is observed to have a pure cubic structure[104,108]. Diez et al. have reported that, the increase in the concentration of Ni in $Ni_xMn_{3-x}O_4$ shows the pure tetragonal (I41/amd) to cubic ($Fd\bar{3}m$) transition when x increases from 0.00 to 1.00 [109]. In general, $CoMn_2O_4$ exhibits a normal spinel structure, with the cationic distribution $(Co^{2+})_A[Mn^{3+}]_BO_4$. Apart from normal spinel, $CoMn_2O_4$ stabilizes as a mixed spinel structure where the random distribution of Co as Co^{2+}/ Co^{3+}/Co^{4+} and Mn as Mn^{2+}/ $Mn^{3+/}$ Mn^{4+} is reported[79,83]. Similarly, various cationic distributions of $MnCo_2O_4$ have also been proposed, such as $Co^{2+}[Co^{2+}Mn^{4+}]O_4$, $Co^{3+}[Mn^{2+}Co^{3+}]O_4$, and $Co^{2+}[Mn^{3+}Co^{3+}]O_4$, depending on the preparation method and calcination temperatures[110]. $Mn_xCo_{3-x}O_4$ with higher Co content is generally described as an inverse spinel in which the Mn cations display a preference for the octahedral sites [8]. The presence of Mn^{3+} in B site is accompanied with Jahn–Teller distortion and lowers the crystallographic symmetry from cubic to tetragonal. This indicates that the crystal structure of $Co_xMn_{3-x}O_4$ is sensitive to Co/Mn ratio and oxidation states. If the cation Mn^{3+} concentration is sufficiently low (60–65%), Jahn–Teller distortion would not be prominent and the spinels could exist in cubic form irrespective of the composition [2]. Besides, for low Co concentration ($0 \leq x < 1.1$), the tetragonal phase exists, while cubic structure is stabilized for high Co content ($1.7 \leq x \leq 3$) [2,75,111,112]. For intermediate Co content, $1.1 \leq x \leq 1.6$, the coexistence of cubic and tetragonal phases is

reported [62,113]. For x = 1.00, although most of the literature shows the pure tetragonal phase, Hosseini et al. have reported the coexistence of tetragonal phase of $CoMn_2O_4$ along with the cubic phase associated with impurity by sol-gel and coprecipitation method. Miyasaka et al., report the pure cubic and tetragonal, depending on the annealing temperature and the SiO_2 content in $CoMn_2O_4$ prepared by a wet chemical synthesis method [26,114]. Apart from XRD, $Co_xMn_{3-x}O_4$ has been structurally characterized by neutron diffraction technique over the whole solid solution range. For $x < 1.75$, ceramics produced at room temperature through conventional sintering methods exhibit tetragonal symmetry, whereas for $x \geq 1.75$ ceramics sintered using Spark Plasma Sintering display cubic symmetry. The unit cells, metal–metal and metal–oxygen average bond lengths consistently decrease as the cobalt content increases. Rietveld refinements of neutron data indicate that cobalt is first preferentially substituted on the A site for $x < 1$, then on the B site for increasing x values. It is also specified that Mn^{2+} and/or Co^{2+} occupy the A site while Mn^{3+}, Co^{2+}, Co^{3+}(cobalt in low-spin state) and Mn^{4+} occupy the B site[102]. In contrast, Li et al., have synthesized $Co_xMn_{3-x}O_4$ where x = 1.00, 1.50 and 2.00 by coprecipitation method in pure cubic and tetragonal structural phase by changing the mixing sequence of Co and Mn precursors. They conclude that change in mixing sequence allow the change in the oxidation states of cations which induces the change in the structure. To determine the oxidation states of mixed metals, X-ray absorption spectroscopy analysis has been performed at the Co and Mn K-edge. Accordingly, the mean Co valence is determined to be 2.25 for c-$CoMn_2$, t-$CoMn_2$ and t-CoMn and 2.38 for c-CoMn, c-Co_2Mn and t-Co_2Mn, where c and t indicates to the cubic and tetragonal phase respectively. A lower Co valence tends to appear in oxides with lower Co content, suggesting an increase in the ratio of Co^{2+}/Co^{3+} due to substitution of Mn cations. As for Mn, the observed average oxidation states for the cubic group (3.28, 3.45, and 3.49 for c-

Co_2Mn, CoMn, and $CoMn_2$) are higher than those for the tetragonal group (2.67, 2.76 and 2.84 for t- Co_2Mn, CoMn and $CoMn_2$). Doping either A or B or both site in $CoMn_2O_4$, affects the structure and cation distribution. Shashidharagowda et al. have studied the A site Cu-doped $CoMn_2O_4$ synthesized through the coprecipitation method. For $Co_{1-x}Cu_xMn_2O_4$, with increase in x from 0.05 to 0.55, cell volume and particle size are found to be increased from 273.96 to 289.04 and 3.93 μm to 13.73 μm, respectively[115] When Cr is doped at the B site of $CoMn_2O_4$, the structural transformation from tetragonal to pure cubic phase has been reported at 80% doping of Cr at B site by using the sol-gel synthesis route [115,116117]. However, Ce doping in $CoMn_2O_4$ doesn't make changes in structure but XPS analysis confirms the change in the ratio of $Co^{3+/}Co^{2+}$, Ce^{3+}/Ce^{4+}, and Mn^{4+}/Mn^{3+} with the Ce doping [117].

1.4.3 Magnetic properties of Co-Mn based spinel

In addition to the structural phase transformations, Co-Mn based spinels show exciting magnetic properties such as ferrimagnetism, Yafet-Kittel type canted antiferromagnetic ordering, highly degenerate magnetic ground states, exchange bias, magnetic switching *etc.*, which have been compiled in the following sections.

With decrease in temperature, these spinels undergo a transition from the paramagnetic (PM) to ferrimagnetic (FIM) phase at Curie temperature, Tc. $Co_xMn_{3-x}O_4$, for x = 0.00, (Mn_3O_4) is a ferrimagnetic spinel showing a triangular spin arrangement as proposed by Yafet and Kittel instead of obeying Neel's antiparallel spin. The temperature (T) dependence of the magnetic susceptibility (χ), investigated by Borovik-Romanov and Orlova[118], indicates Mn_3O_4 to be a ferrimagnet with Tc = 42 K. Magnetic investigations on a powder sample by Jacobs and on a single crystal by Dwight and Menyuk matches with the above studies. They observe magnetic ordering below Tc which is not collinear

or Neel type, but consists of a canted arrangement of Yafet-Kittel type [119,120]. In Mn_3O_4, when A sites are replaced with non-magnetic ions like Zn or Mg, a magnetic dilution effect can be observed resulting in weak exchange interactions [106,107] . On the other hand, when magnetic ions like Fe/Ni/Co are substituted, the complex magnetic behavior is detected which may be related to competing exchange interaction between both the lattice sites [24,103–105]. The $Mg_xMn_{3-x}O_4$ system shows a ferrimagnetic phase, but with an increase in x as the substitution of Mn^{2+} ions by non-magnetic Mg^{2+} ions at the A site, the ferrimagnetic features decline drastically in the range $0 \leq x \leq 0.4$. This points out that the Mn^{2+} ions at the A site are responsible for the ferrimagnetic order in Mn_3O_4. Moreover, the substitution of Mn^{2+} by Mg^{2+} modifies the interactions J_{AA}, J_{AB} and J_{BB} so that the long-range ferrimagnetic order evolves into a magnetic frustration state of the B-sublattice, in the region $0.5 \leq x \leq 0.9$. Finally, a spin-glass phenomenon is detected in the cubic domain in the range $1.5 \leq x \leq 2$. With the increase in x from 0 to 2, Tc is found to be continuously decreasing from 42.6 to 12 K [106.] For $Zn_xMn_{3-x}O_4$, the results of the magnetic properties are found in good agreement with the model based on the coexistence of ferrimagnetic nanoscale clusters of Mn_3O_4 in the antiferromagnetic $ZnMn_2O_4$ matrix. In Mn_3O_4 (Tc = 42 K), $Zn_{0.3}Mn_{2.7}O_4$ (Tc = 32 K) and $Zn_{0.45}Mn_{2.55}O_4$ (Tc = 25 K) spinels the bulk ferrimagnetic state is observed, and for $Zn_{0.75}Mn_{2.25}O_4$ the results point to the short-range ferrimagnetic ordering. H_C is found to be maximum (2870 Oe) for Mn_3O_4 which is found to be decreased and become 5 Oe for $Zn_{0.75}Mn_{2.25}O_4$ [107] .

Magnetic ion doping in Mn_3O_4 highly affects the magnetic properties like magnetic interactions among the sublattices, spin interactions as well as curie temperatures. On Fe doping in Mn_3O_4, curie temperatures are observed to increase significantly from 41.8 K to 413 K in Mn_2FeO_4, to 563 K in $MnFe_2O_4$, and 858 K in Fe_3O_4 [121]. Ni doping in Mn_3O_4 results in an increase in Tc, hence a ferrimagnetic transition

is identified at ≈100 K for $NiMn_2O_4$ with a ferrimagnetic moment of ≈1μB [109]. When Mn_3O_4 is doped by Co the magnetic properties become more complex. In evidence to this for $Co_xMn_{3-x}O_4$, two magnetic transitions (higher transition temperature (Tc_1) and lower transition temperature (Tc_2)) are observed for x =1.00 ($CoMn_2O_4$), where both are found at higher temperature than observed for Mn_3O_4[103,105,121]. $CoMn_2O_4$ synthesized through the combustion method shows two magnetic transitions Tc_1 and Tc_2 at 184 and 74 K[83], respectively. Transition temperatures of $CoMn_2O_4$ prepared through the different methods with particle size are shown in **Table 1.3**. From the table, one may conclude that these transition temperatures Tc_1 and Tc_2 can vary from 165 to 190 K and 78 to 90 K, respectively. The high temperature transition may be attributed to a small impurity (~ 5%) phase that could be related to one of the phases within the $Co_xMn_{3-x}O_4$ system[102,110]. Mehata et al. have reported that reducing the particle size (from bulk to nano) in this system seems to vanish the high temperature transition, which indicates that the secondary phase (associated with the Co_3O_4) may not exist in the small particles of the $CoMn_2O_4$ spinels[122]. On the other hand, low temperature transition (Tc_2) with a very high magnetization infers the existence of long-range magnetic ordering. In a report by Boucher et al., on cobalt manganite single crystals, this transition is caused by the presence of Yafet–Kittel spin structures [103]. Below Tc_2, Mn^{3+} ions present in the B sites have achieved a non-collinear triangular spin canting arrangement, which leads to ferrimagnetic moments. Above Tc_2, there is a vanishing effect of these noncollinear moments among Mn^{3+} ions, and thus a drop in magnetization in the M–T curve has been observed. Mn^{3+} ions present in the B sites must be the cause for these Yafet–Kittel spin structures, as spins of Co^{2+}/Mn^{2+} occupying the tetrahedral sites are always collinear[83]. Apart from this for $CoMn_2O_4$, coercivity is found to have a large variation from 2850 Oe to 2000 Oe depending on synthesis method[78,83,123]. Zhang et al. have observed the

blocking temperatures in the range of 30–40 K which do not increase with particle size, partially due to the broad metastable cation distribution and partially because of the dipolar interactions among the nanoparticles. In addition, they also have observed the exchange bias of 30, 650 and 643 Oe for 5.3, 6.7 and 9 nm sized $CoMn_2O_4$ nanoparticles, respectively, due to the ferrimagnetic–ferromagnetic exchange coupling among the ferrimagnetic core and ferromagnetic shell [124]. In contrast to $CoMn_2O_4$, $MnCo_2O_4$ shows single magnetic transition for both bulk and nanoparticle tabulated in **Table 1.3**. From the table, it is confirmed that with decreasing the particle size from bulk to nanometer, Tc is found to be decreased. Several studies indicate the interesting phenomenon observed in $MnCo_2O_4$. Tamura et al. have studied the pressure dependence of magnetic permeability for polycrystalline $MnCo_2O_4$ [125]. For $T < T_C$ (185 K), the relative magnetic permeability $\mu_r(T)$ shows a peak at $T_H = 175$ K owing to the Hopkinson effect in which both T_H and Tc decrease linearly with pressure increasing from 0 to 1.71 GPa [125,126]. Joy and Date have observed that $MnCo_2O_4$ shows anomalous magnetic M-H behavior below 130 K where the virgin magnetization curve at higher fields lies outside the main M-H loop[127] . Bazuev et al. have observed the magnetic behavior in $MnCo_2O_{4+\delta}$ ($\delta = 0.275$ and 0.62) spinel prepared through thermal decomposition of binary oxalates $Mn_{1/3}Co_{2/3}C_2O_4 \cdot 2H_2O$ at 220 ºC and 500 ºC[128]. For $\delta = 0.275$, $d\chi/dT$ versus T curve displays a minimum across 167.5 K below $T_C \sim 183$ K for stoichiometric spinel $MnCo_2O_4$ [128]. Apart from this, Thota et al. have reported a reduced T_C at 176 K and spin-glass like phenomenon across 165 K with the magnetic memory and relaxation phenomena in 28 nm average-sized $MnCo_2O_4$ nanocrystallites [129]. So far, we have briefly discussed the magnetic properties of Mn_3O_4, and doped Mn_3O_4, where $CoMn_2O_4$ needs to be taken special attention for having the unusual two magnetic transitions. There are only a few reports on the magnetic properties of doped $CoMn_2O_4$. $Co_{1-x}Cu_xMn_2O_4$

demonstrates an increase in ferromagnetism as Cu substitution increases, which relies upon ionic size and cation distribution[115]. Interesting magnetic properties have been reported when Co is present at A site, Cr and Mn are present at B site i.e., $Co(Cr_{1-x}Mn_x)_2O_4$ ($0 \leq x \leq 0.6$). It is found that Cr with Mn induces the negative magnetization in the range of $0.3 \leq x \leq 0.5$. The negative effect arises from the competition between two magnetic sublattices at different crystallographic sites. For x = 0.3, the magnetic switching behaviour near the compensation temperature T_{comp} has been observed, and it exhibits potential applications in spintronic devices. Apart from this, both the positive and negative exchange bias effects are obtained, which are attributed to the pinning force of uncompensated spins on ferromagnetic moments and the magneto-structural transition, respectively[116]. On the other hand for $Co(Cr_{1-x}Mn_x)_2O_4$ ($0 \leq x \leq 0.3$), Kumar et al. have reported the tuning of magnetic structure and its effect on magnetic compensation temperature (T_{comp}) and then the onset of negative magnetization at T = 60 K and 83 K, for x = 0.27, and x = 0.30. Magneto-elastic coupling near compensation temperature is observed, which results in the sign change of the magneto-caloric effect at compensation temperature[130].

Table 1.3: Transition temperature of $CoMn_2O_4$ and $MnCo_2O_4$ prepared through different method with particle.

Composition	Method of preparation	Particle size	Transition temperature		References
			High temperature transition	Low temperature transition	
$CoMn_2O_4$	Combustion process	150 nm	184	74	[83]
$CoMn_2O_4$	Thermal decomposition	8	-	87	[80]
		18	167.5	86.3	
		30	177.7	82.3	
		40	183.4	78.9	
$CoMn_2O_4$	Thermal decomposition	31 nm	180	83	[78]
$CoMn_2O_4$	Solid state reaction Method	bulk	185	90K	[131]
$CoMn_2O_4$	Quenching at 1250	bulk	100	-	[103]
$CoMn_2O_4$	Thermal decomposition	bulk	190	90	[122]
$MnCo_2O_4$	High temperature quenching	Bulk	185	-	[125]
$MnCo_2O_4$	Pechini method	50 nm	174.8	-	[132]
$MnCo_2O_4$	sol-gel process	28	165	-	[129]

1.5 Objectives

In Co-Mn based spinel oxides, Co and Mn both can occupy A and B site exhibiting multiple valences, thus having tunable structural phases. In $Co_xMn_{3-x}O_4$, structural transformation from tetragonal (space group $I41/amd$) to cubic phase (space group $Fd\bar{3}m$) with increase in x has been observed. Presence of Mn^{3+} in B site is accompanied with Jahn–Teller distortion in octahedral interstices and lowers the crystallographic

symmetry from cubic to tetragonal. This indicates that the crystal structure of $Co_xMn_{3-x}O_4$ is sensitive to Co/Mn ratio and occupancy among A or/and B site. Overall, there are only few reports which show Co/Mn ratio and their occupancy among A or/and B sites by advanced technique such as XAFS, to explain systematic structural transformation. In addition to this, very less attention has been paid to structure dependent magnetic properties in $Co_xMn_{3-x}O_4$ spinels which exhibit a complex magnetic behaviour showing magnetic ordering at low temperatures. In Mn_3O_4 (x = 0.00), with substitution of Mn by Co, exchange interaction between triangular spin arrangement of Mn^{3+} at B site and collinear spin arrangement of Co^{2+}/Mn^{2+} at A site induces more complexity in their magnetic behaviour. Generally, two transitions have been observed in $CoMn_2O_4$, where the low temperature transition is related to the tetragonal phase and the high temperature transition is assigned to some impurity phase. There is a scarcity of reports explaining the second transition observed in M vs T curve and other magnetic phenomenon commonly observed in spinel. Apart from this, presence of Cr at B site of spinel induces the interesting magnetic properties like negative magnetization and magnetic reversibility. Henceforth, primary objective of this work is to investigated thoroughly the structure microstructure and local structure and their correlation with magnetic properties of $Co_xMn_{3-x}O_4$ with varying x from 1.00 to 2.00 and Cr.

In this chapter, a concise overview of spinel, elucidating its structure, compositions, properties, and brief literature survey on spinel, $Co_xMn_{3-x}O_4$ and the effect of dopants on $Co_xMn_{3-x}O_4$ is presented. Based on the literature survey, the objective of the thesis is outlined accordingly.

In Chapter 2, we present the methodology utilized for sample preparation. The chapter also addresses characterization techniques like XRD, XAFS, RAMAN, XPS, SEM, TEM, and MPMS that are used for data collection and analysis.

Based on the literature survey our objective of Chapter 3 is to synthesize $CoMn_2O_4$ nanoparticles and explain the magnetic transitions and the magnetic phenomena like vertical magnetization shift and exchange bias in correlation with structure.

After observing the interesting structural properties in $CoMn_2O_4$ our primary objective of Chapter 4 is to synthesize $Co_xMn_{3-x}O_4$ with varying x from 1.00 to 2.00, and investigate thoroughly the structure microstructure and local structure by well-known techniques and advanced characterization technique i.e., XAFS.

After observing the exciting structural transformation in $Co_xMn_{3-x}O_4$, the aim of Chapter 5 is to study the magnetic properties and establish the correlation of structure and local structure with magnetic properties in $Co_xMn_{3-x}O_4$ with varying x from 1.00 to 2.00.

Since doping has a significant effect on the properties of spinel therefore in Chapter 6, we will examine the structure-properties correlation, especially emphasizing magnetic properties after Cr doping in $CoMn_2O_4$ as Cr^{3+} occupies B site, similar to Co^{3+} prefers *B* site with increase in x in $Co_xMn_{3-x}O_4$.

In Chapter 7, we have summarized the important findings of this thesis work, along with a discussion of future prospects.